Materialia 11 (2020) 100696

Contents lists available at ScienceDirect

Materialia

journal homepage: www.elsevier.com/locate/mtla

Influence of spinodal decomposition and fcc→w phase transformation on global and local mechanical properties of nanolamellar CVD fcc-$Ti_{1-x}Al_xN$ coatings

Michael Tkadletz[a,*], Alexandra Lechner[a], Nina Schalk[a,b], Bernhard Sartory[c], Andreas Stark[d], Norbert Schell[e], Christian Saringer[b], Christian Mitterer[a], Christoph Czettl[a]

[a] Department of Materials Science, Montanuniversität Leoben, Franz Josef-Straße 18, 8700 Leoben, Austria
[b] Christian Doppler Laboratory of Advanced Coated Cutting Tools, Montanuniversität Leoben, Franz Josef-Straße 18, 8700 Leoben, Austria
[c] Materials Center Leoben Forschung GmbH, Roseggerstraße 12, 8700 Leoben, Austria
[d] Institute of Materials Research, Helmholtz-Zentrum Geesthacht, Max-Planck-Straße 1, 21502, Geesthacht, Germany
[e] CERATIZIT Austria GmbH, Metallwerk-Plansee-Straße 71, 6600 Reutte, Austria

ARTICLE INFO

Keywords:
In situ
Synchrotron radiation
Phase composition
Nanoindentation
CVD TiAlN

ABSTRACT

Recently, it was shown that annealing of nanolamellar CVD fcc-$Ti_{1-x}Al_xN$ at temperatures of 1000-1200 °C results in the formation of complex phase fields consisting of still intact nanolamellar face centered cubic (fcc) zones, side by side with non-lamellar fully decomposed and transformed fcc and wurtzite (w) zones. It can be assumed that the observed phase fields and their microstructure strongly correlate with their mechanical properties. Consequently, this work focuses on the investigation of the effects of spinodal decomposition and fcc→w phase transformation of a nanolamellar CVD fcc-$Ti_{0.2}Al_{0.8}N$ coating on the corresponding global and local mechanical properties. The sequence of spinodal decomposition and fcc→w phase transformation of a compact coating sample was investigated by *in situ* high temperature synchrotron X-ray diffraction up to a maximum temperature of ~1250 °C. Conventional nanoindentation experiments on the surfaces of samples annealed between 900 to 1300 °C in vacuum were performed to illustrate the age hardening and overaging behavior. Finally, the influence of the observed phase fields on the local mechanical properties was investigated by correlative SEM/EBSD and nanomechanical mapping experiments on a cross-section of a coating annealed at 1050 °C. Maps of the lateral microstructure, phase composition, Young´s modulus and hardness of the coating were successfully obtained with a resolution of ≤100 nm. The lateral phase fields could be clearly identified and correlated with the observed mechanical properties. The results indicate that age hardening of nanolamellar CVD fcc-$Ti_{0.2}Al_{0.8}N$ coatings occurs homogeneously, while overaging is associated to the fcc→w transformation and thus, locally confined.

1. Introduction

In the last decade, chemical vapor deposited (CVD) Al-rich $Ti_{1-x}Al_xN$ coatings for cutting tools in the machining industry have been subject of extensive research [1–13]. Although thermally activated CVD coatings are usually assumed to grow close to their thermodynamic equilibrium state, metastable purely face-centered cubic (fcc)-$Ti_{1-x}Al_xN$ coatings with relatively high Al-content can be realized utilizing this technique [1,4,8,10,13]. A unique feature of those Al-rich CVD fcc-$Ti_{1-x}Al_xN$ coatings, that has been repeatedly reported, is the formation of a self-assembled nanolamellar microstructure of alternating Al-rich and Ti-rich lamellae with a periodicity of several nm [4,6,8,14]. The high global Al-content of such coatings results in a superior oxidation resistance and hardness which, in combination with the unique microstructure, yields superior cutting performance compared to conventional fcc-$Ti_{1-x}Al_xN$ coatings [1–4,9,10,13].

Although the microstructural evolution of metastable fcc-$Ti_{1-x}Al_xN$ coatings at elevated temperatures is of major relevance for age hardening and subsequent overaging, which has been extensively investigated for physical vapor deposited (PVD) $Ti_{1-x}Al_xN$ coatings in the last decades, there are only a few studies for the CVD counterpart so far. Early studies by Endler et al. [1,2,10] reported on annealed Al-rich CVD fcc-$Ti_{1-x}Al_xN$ coatings, not of explicitly nanolamellar type at this point, indicating spinodal decomposition and subsequent fcc→wurtzite (w) phase transformation. Later, Todt et al. [4] and Köpf et al. [13] showed pronounced age hardening and subsequent overaging of explicitly nanolamellar CVD fcc-$Ti_{1-x}Al_xN$ and provided a comparison to PVD coatings. Todt et al. [4] as well as Paseuth et al. [6] confirmed

* Corresponding author.
E-mail address: michael.tkadletz@unileoben.ac.at (M. Tkadletz).

https://doi.org/10.1016/j.mtla.2020.100696
Received 7 April 2020; Accepted 12 April 2020
Available online 12 May 2020

decomposition and subsequent fcc→w phase transformation of nanolamellar CVD fcc-$Ti_{1-x}Al_xN$ coatings by *ex situ* investigations on annealed samples. However, while the phase evolution during decomposition and fcc→w transformation might be satisfyingly revealed by *ex situ* approaches, a thorough illustration of the strain and strain free lattice parameter evolution during annealing can only be provided by *in situ* experiments. Recent studies covered *in situ* high temperature X-ray diffraction (HT-XRD) experiments performed on compact samples, but missed to reach temperatures high enough to cover the whole sequence of decomposition and fcc→w phase transformation [7,15]. Consequently, the governing mechanism for age hardening and subsequent overaging of nanolamellar CVD fcc-$Ti_{1-x}Al_xN$ coatings, in particular the role of the individual lamellae, is still not fully described.

Recently, the authors investigated the thermal stability of a nanolamellar CVD fcc-$Ti_{0.2}Al_{0.8}N$ coating by *in situ* synchrotron HT-XRD experiments using a powdered sample of the coating. The obtained results were compared with *ex situ* experiments on compact samples [8]. This work provided a comprehensive description of the spinodal decomposition and fcc→w transformation sequence of nanolamellar Al-rich CVD fcc-$Ti_{1-x}Al_xN$ coatings. After annealing at intermediate temperatures between 1000-1200 °C, intact nanolamellar fcc areas were found, coexisting side by side with non-lamellar fully decomposed and transformed fcc+w zones. Accordingly, it can be assumed that the observed phase fields determine the local mechanical properties of such coatings. As a consequence, the global mechanical properties, such as Young´s modulus and hardness, obtained by nanoindentation experiments on the coating surface might not represent a thorough image of the nanomechanical properties of such samples.

The intention of this work is, on the one hand, to confirm our previously proposed decomposition and transformation sequence [8] and on the other hand, the investigation of global as well as local effects of the observed phase fields on the nanomechanical properties of nanolamellar Al-rich CVD fcc-$Ti_{1-x}Al_xN$ coatings. Thus, a compact CVD fcc-$Ti_{0.2}Al_{0.8}N$ coating sample was investigated up to a temperature of ~1250 °C using *in situ* synchrotron HT-XRD. Surface nanoindentation measurements on polished coating surfaces of six samples, annealed in vacuum at different temperatures ranging from 900 to 1300 °C, were performed. In addition, a coating cross-section of a sample annealed at 1050 °C, exhibiting intact nanolamellar as well as decomposed and transformed fcc+w areas, was prepared and documented by means of scanning electron microscopy (SEM) and electron backscatter diffraction (EBSD). Subsequently, dynamic-elastic modulus mappings and quasi-static elastic-plastic indentation mappings were collected with a resolution ≤100 nm and cross-correlated with the SEM and EBSD results.

2. Experimental methods

The nanolamellar Al-rich CVD fcc-$Ti_{1-x}Al_xN$ coating investigated within this work was deposited with an industrial scale CVD reactor of type Sucotec SCT600TH using $TiCl_4$, $AlCl_3$, NH_3, H_2, N_2 and Ar as precursors. Cemented carbide samples, pressed and sintered to SNUN 120412 geometry (according to ISO 1832), with a composition of 92 wt.% WC, 6 wt.% Co and 2 wt.% mixed carbides, served as substrates. Prior to deposition of the ~2.5 µm thick fcc-$Ti_{0.2}Al_{0.8}N$ coating, a ~400 nm thick fcc-TiN baselayer was deposited to prevent interdiffusion between coating and substrate. For the deposition of the fcc-$Ti_{0.2}Al_{0.8}N$ coating, the $AlCl_3$:$TiCl_4$ ratio was set to 6.1:1, at a deposition temperature of 790 °C and a total pressure of 4.5 kPa. The total gas flow was 101 l/min, resulting in a deposition rate of ~1 µm/h [8,9,16].

In situ synchrotron HT-XRD measurements were performed at the high energy materials science beamline P07 at DESY (PETRA III, Hamburg, Germany) up to a temperature of ~1250 °C in high vacuum applying a heating rate of 10 $Kmin^{-1}$. The sample was heated inductively via the substrate and the temperature was controlled by a thermocouple directly welded to the substrate material. Diffraction patterns were collected in steps of ~2 °C in transmission geometry using a 2D detector, a photon energy of 87.1 keV and an X-ray beam size of ~400 × 100 μm^2 (long axis aligned parallel to the coating interface). For phase analysis and lattice parameter evaluation, the strain free directions [17] of the recorded diffraction images were integrated along the azimuthal direction and resulting diffractograms were analyzed by means of a sequential peak fitting procedure using the software Bruker Topas 6. The macroscopic lattice strains were estimated from the distortion of the Debye-Scherrer rings, as described in Ref. [18].

Different stages of decomposition and fcc→w transformation were reproduced by annealing in vacuum at 900, 1000, 1050, 1100, 1200 and 1300 °C, for 5 minutes each. A HTM RETZ high vacuum furnace operated at a base pressure < 5×10^{-4} Pa was used to anneal the samples, applying a heating rate of 20 °C/min and a system dependent cooling rate [8]. Nanoindentation experiments on the surface of the annealed samples were performed to investigate the global hardness and reduced modulus using a UMIS nanoindentation system provided by Fischer-Cripps Laboratories. On each sample, 25 individual indents in a load range of 15-25 mN were conducted, resulting in an indentation depth of ~140-200 nm, corresponding to less than ~10 % of the fcc-$Ti_{0.2}Al_{0.8}N$ coating thickness.

XRD measurements for phase analysis of the as deposited coating as well as the coatings annealed at 1050 °C and 1200 °C were carried out using a Bruker D8 Advance diffractometer. The diffractometer was equipped with a Cu Kα X-ray tube (λ= 1.5418 Å), parallel beam optics (i.e. Göbel mirror), a secondary equatorial Soller collimator (0.12° acceptance) and an energy dispersive Sol-X detector. Scans were performed from 20-85° 2θ, using grazing incidence mode at an incidence angle of 2° and a step size of 0.02° [8]. A Zeiss Auriga 40 Crossbeam SEM, equipped with an EDAX Hikari XP Super EBSD camera and an Orsay Physics Cobra Z-05 focused ion beam (FIB) extension was applied for cross-sectional SEM and EBSD investigations of the as deposited coating and the coating annealed at 1200 °C. Cross-correlative SEM/EBSD investigations and cross-sectional nanomechanical measurements of the coating annealed at 1050 °C were carried out on a coating cross-section. For those experiments, special attention has to be paid to the sample preparation. Thus, the sample was sputter coated with a ~1 µm thick Au protective layer prior to preparation, which avoids edge rounding and results in decreased curtaining (i.e. roughness) and other focused ion beam (FIB) artifacts during the preparation process. Further, it provided mechanical support for the indenter tip, beyond the coating surface, during scanning probe microscopy (SPM) imaging and subsequent indentation testing. After deposition of the protective Au layer, a preliminary coating cross-section was prepared by broad Ar^+ ion beam polishing using a Hitachi IM4000+ ion milling system. The broad Ar^+ ion beam polishing was followed by final FIB polishing of an area of ~20 µm width at low beam currents, after deposition of an additional ~0.4 µm thick Pt layer on top of the region of interest (ROI), using the Zeiss Auriga 40 crossbeam SEM/FIB. For improved navigation/orientation during SPM imaging and subsequent image correlation, the FIB polished area was additionally referenced by two “X” shaped markers within the substrate region, on the left and right hand side of the ROI. After preparation of the coating cross-section, the ROI was documented by SEM imaging and EBSD mapping using a Zeiss Gemini SEM 450 quipped with an Oxford Systems Symmetry EBSD camera. After documentation, prior to the nanomechanical experiments, the coating cross-section was plasma cleaned for 12 h using an Evactron Zephyr 25 plasma cleaner.

Nanomechanical testing on the prepared coating cross-section was performed utilizing a Hysitron TI 950 TriboIndenter equipped with a Perfomech control module, a nanoDMA transducer and a Northstar diamond cube corner indenter. Prior to modulus mapping measurements, the sample was aligned using continuous SPM imaging. After alignment, a 4 × 4 μm^2 SPM image of the ROI was captured. During modulus mapping, the dynamic load amplitude was set to yield a dynamic displacement amplitude of ~0.3-0.6 nm within the $Ti_{0.2}Al_{0.8}N$ coating. After collection of three individual image sets (gradient, topography, phase and amplitude), the corresponding modulus maps were calcu-

lated. For quasistatic indentation testing, an array of 35 × 50 indents with a spacing of 100 nm was aligned to cover the ROI, resulting in a total map size of ~3.5 × 5 μm^2 with a total number of 1750 indents. The indentation measurements were performed applying a constant maximum load of 200 μN, yielding a contact depth of ~20-30 nm, depending on the particular position and the corresponding encountered phase field. Prior and after mapping, the indenter tip was calibrated within the utilized contact depth range, using a fused silica standard reference sample (reduced modulus of E_r = 69.6 GPa). The obtained area functions were reviewed within the calibrated range by succeeding independent reference measurements. Subsequently, the mapping results were evaluated using pre- and post-map area functions and interpolated accordingly.

The applied load and indent spacing were selected to result in a clear separation of the individual indents, where the indent spacing was ~2-3 times the width of the residual imprint of the indents, which has been recently reported as sufficient criterion to yield proper quantitative mapping results [19,20]. To verify this criterion, a 5 × 15 array of indents was made on a fused silica sample with same spacing but an adjusted peak load of 50 μN, yielding a similar contact depth (~20 nm) and thus comparable conditions for evaluation of the influence of the narrow indentation spacing on the quantitative evaluation. In addition, the influence of tip wear occurring during the extensive mapping procedure was evaluated by a post-map fused silica measurement, within the observed contact depth range, using the initial tip area function. Both measurements revealed hardness and reduced modulus data lying within 5 % of the expected reference values, indicating that neither the narrow indent spacing nor pronounced tip wear were of any concern for the performed experiment.

3. Results and discussion

3.1. In situ *investigations of microstructural and strain evolution during annealing*

The phase evolution versus temperature obtained during the *in situ* synchrotron experiment is depicted by the contour plot shown in Fig. 1a. The corresponding normalized phase intensity can be found in Fig. 1b. Both confirm the findings of our previous work for the sequence of decomposition and subsequent fcc→w phase transformation of CVD fcc-$Ti_{1-x}Al_xN$ coatings [8]. Up to a temperature of ~950 °C, i.e. ~150 °C above deposition temperature, the fcc microstructure is still intact and no major changes – except the peak shift to lower values – in the phase composition are observed. As the temperature further rises, between 950-1150 °C, increasing intensities of fcc-TiN[1] and w-AlN[1] in the contour plot in Fig. 1a, as well as in the intensity plot in Fig. 1b are observed, while fcc-$Ti_{0.2}Al_{0.8}N$[2] significantly decreases. This clearly indicates spinodal decomposition and subsequent fcc→w transformation. Above ~1150 °C, the fcc-$Ti_{0.2}Al_{0.8}N$ has completely decomposed and transformed into fcc-TiN and w-AlN.

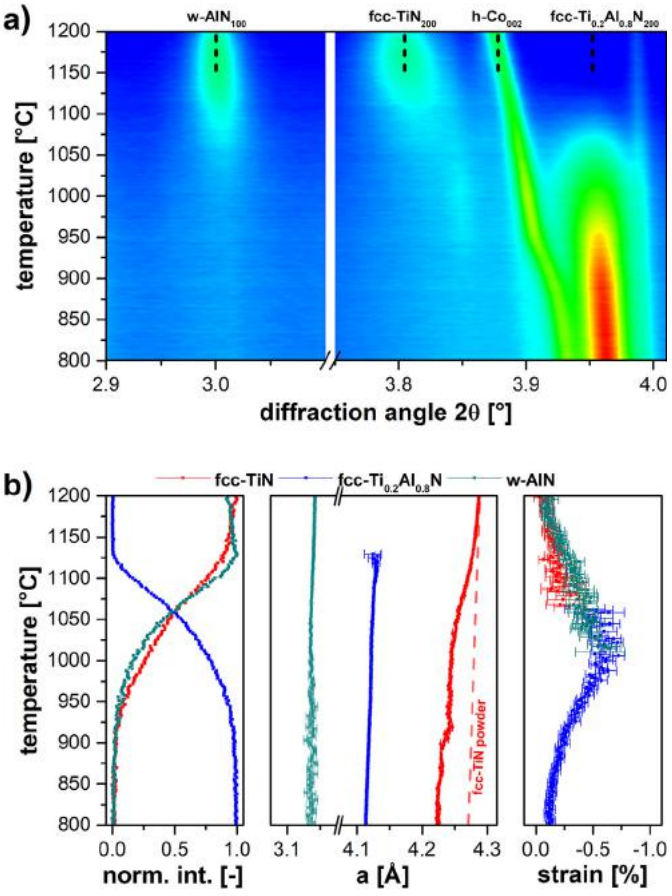

Fig. 1. Phase evolution versus temperature (a) and normalized phase intensities, strain free lattice parameters and macroscopic lattice strain (b) of a CVD fcc-$Ti_{0.2}Al_{0.8}N$ coating determined using *in situ* synchrotron HT-XRD.

Throughout the whole sequence of spinodal decomposition and fcc→w transformation, the lattice parameters of fcc-$Ti_{0.2}Al_{0.8}N$ and w-AlN, shown in Fig. 1b, exhibit their expected positions. A minor, almost linear increase with temperature that can be related to the inherent thermal expansion of the phases is observed. Only the lattice parameter of the Ti-rich phase constituents formed during spinodal decomposition initially reveal a lattice parameter which is significantly shifted towards fcc-AlN. This implies that these phase fractions still contain a considerable amount of Al in the beginning. With increasing temperature, a strong non-linear shift towards the expected position of fcc-TiN is observed, indicating out-diffusion of AlN. The shift proceeds until the lattice parameter of pure fcc-TiN is reached at ~1150 °C, evidencing that spinodal decomposition and fcc→w transformation are completed. For better identification of the described shift, the lattice parameter versus temperature of pure fcc-TiN is depicted by a dashed line in Fig. 1b. The corresponding data was determined using a powdered CVD fcc-TiN coating.

The evolution of the macroscopic lattice strain, presented in Fig. 1b, shows a clear correlation with the observed phase evolution and gives a first indication about the age hardening behavior of the coating. The coating in the as deposited state revealed tensile strains which would correspond to a tensile residual stress of ~1450 MPa, if X-ray elastic constants according to the Neerfeld-Hill approximation are considered for the given global chemical composition [21–23]. This is in good agreement with the findings of Paseuth et al. who reported values of similar magnitude for a nanolamellar CVD fcc-$Ti_{0.18}Al_{0.82}N$ coating [7]. Upon heating, a transition from tensile to compressive strain was found at the deposition temperature of ~790 °C. At ~950 °C, the coating already

[1] Due to a certain degree of mutual solubility, the decomposition and transformation products of fcc-$Ti_{1-x}Al_xN$ are usually rather considered as Ti-rich fcc-(Ti,Al)N and Al-rich w-(Al,Ti)N than fcc-TiN and w-AlN, in particular for intermediate stages of decomposition and transformation. Nevertheless, for simplicity, the newly formed phase fractions are referred to as fcc-TiN and w-AlN within this manuscript.

[2] In a previous work [8] the authors showed that diffractogramms of nanolamellar CVD fcc-$Ti_{1-x}Al_xN$ coatings can be desribed by two fcc phases with slightly different lattice parameter. One representing Ti-rich and the other representing Al-rich constituents of the nanolamellar structure, these were consequently referred to as fcc-(Ti,Al)N and fcc-(Al,Ti)N, respectively. However, within the present work, due to the different setup and a possible overlap of the fcc-$TiAlN_{200}$ and h-Co_{002} reflections throughout decomposition, a strict differentiantion of both constituents was not possible. Thus the predominant fcc phase is simply referred to as fcc-$Ti_{0.2}Al_{0.8}N$.

exhibits moderate compressive lattice strain of ~0.1 %, which would correspond to compressive residual stress of ~350 MPa, if calculated using room temperature X-ray elastic constants. Since it can be assumed that the coating is primarily subjected to thermal stress as long as no phase transformations occur, this value seems rather reasonable for a CVD coating upon heating above deposition temperature, considering the mismatch in thermal expansion coefficients of substrate and coating [24]. In this context, also an influence of the TiN baselayer might be assumed due to the slightly different thermal expansion of TiN and $Ti_{1-x}Al_xN$ [25]. However, since the difference in thermal expansion between the two layers is significantly less than the difference between the coating layers and substrate, the influence of the comparatively thin (0.4 μm) baselayer is supposedly small. Further, CVD TiN does neither show phase transformations nor pronounced recovery or relaxation within the investigated temperature range [26], thus the strain offset caused by the TiN baselayer will be constant and is assumed to be smaller than the actual measurement error. The linear behavior instantly changes as spinodal decomposition sets in, which results in a pronounced increase in compressive residual strain, reaching its maximum of ~0.6 % at ~1000 °C, corresponding to a compressive stress of about ~2000 MPa, estimated in the same way as above. Although shifted towards higher process-related negative strains, a similar behavior was previously reported for PVD $Ti_{1-x}Al_xN$-based hard coatings, which had, however, a much lower Al-content [27,28]. By means of phase field simulations it could be shown that upon spinodal decomposition of fcc-$Ti_{1-x}Al_xN$ into fcc-TiN and fcc-AlN only minor changes in the observed strain can be expected [28]. Subsequently, the initial formation of w-AlN domains, which obtain a larger molar volume compared to fcc-TiAlN and fcc-TiN, were considered to significantly increase the compressive strains and thus the hardness of the investigated coatings, as already suggested earlier by other authors [29,30]. However, upon further annealing, the maximum in compressive strain decreased again, which was related to the increasing size of w-AlN domains [28]. Consequently, the significant increase in compressive strain of the coating investigated within this work is interpreted as an indication for pronounced age hardening, which is expected to show its maximum at a temperature of ~1000 °C. In accordance with the works discussed above [27,28], the strong increase in compressive strain is observed as long as a predominantly fcc-$Ti_{0.2}Al_{0.8}N$ matrix is present. At higher temperatures, the compressive strains decrease again as the fcc→w transformation proceeds. At this point, the matrix can be assumed to predominantly consist of w-AlN, which accommodates domains of fcc-TiN and some remaining fcc-$Ti_{0.2}Al_{0.8}N$. Accordingly, the maximum in compressive strain can be assumed to define the border line between age hardening and overaging, since decreasing strain and increasing w-phase fraction results in a pronounced reduction of the hardness [31]. Above 1150 °C, neither the phase composition nor the lattice parameters nor the strain do change significantly anymore. Due to the relatively high global Al fraction of the coating and in accordance with our previous findings [8], it can be assumed that a w-AlN matrix with embedded fcc-TiN globules is formed, representing the fully decomposed and transformed microstructure. A further increase in annealing temperature primarily affects the shape and size of fcc-TiN globules within the w-AlN matrix due to ongoing recrystallization and growth of the precipitates. The obtained results indicate, that despite the substantially different chemical composition and microstructure in the as deposited state, and some process related differences in the magnitude of the initial strain, the evolution of strains and thus very likely also the age hardening behavior of state-of-the-art PVD and CVD $Ti_{1-x}Al_xN$ are comparable.

3.2. *Ex situ investigations of microstructural evolution within selected samples after annealing*

In addition to the *in situ* synchrotron HT-XRD experiment, three representative microstructural states, i.e. as deposited state, intermediate state annealed at 1050 °C and fully decomposed and transformed

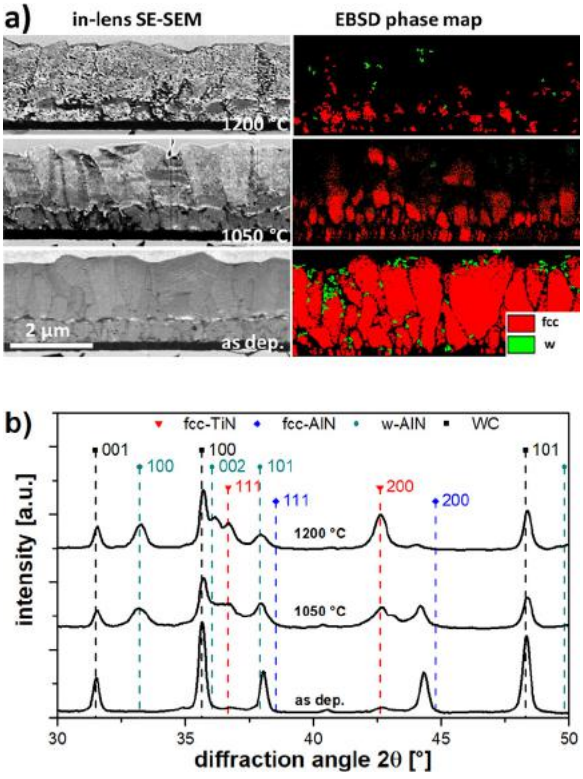

Fig. 2. In-lens SE-SEM images and EBSD phase maps (a) and corresponding *ex situ* diffractograms (b) recorded from the as deposited state, the intermediate and the final state of a CVD fcc-$Ti_{0.2}Al_{0.8}N$ coating after annealing for 5 min in vacuum, respectively.

state annealed at 1200 °C, were investigated by means of SEM, EBSD and *ex situ* XRD. The respective results are summarized in Fig. 2a and b. At the bottom of the in-lens secondary electron (SE) SEM images shown in Fig. 2a, the ~0.4 μm thick fcc-TiN baselayer and the ~2.5 μm thick $Ti_{0.2}Al_{0.8}N$ coating can be clearly identified. For all microstructural states, the initial $Ti_{0.2}Al_{0.8}N$ microstructure with grain sizes in the lower micrometer range can still be observed. Within the $Ti_{0.2}Al_{0.8}N$ layer, a discontinuity at ~1/3 of the coating thickness is visible, which was caused by process instabilities as described previously [8]. However, this instability did obviously not affect further growth of the initial fcc-$Ti_{1-x}Al_xN$ structure, as evidenced by the EBSD phase map of the as deposited state shown in Fig. 2a. The EBSD phase map as well as the XRD pattern (Fig. 2b) of the as deposited coating reveal a predominant fcc structure with only insignificant amounts of w-phase. For easier phase identification, standard peak positions taken from respective ICDD PDF cards for fcc-TiN, fcc-AlN, w-AlN and WC are provided within the diffractograms in Fig. 2b [32–35]. The intensity of fcc-TiN observed in the as deposited coating can be related to the baselayer, WC peaks stem from the substrate.

As expected from the *in situ* synchrotron HT-XRD experiment, the coating annealed at 1050 °C appears somewhat inhomogeneous in the in-lens SE-SEM image, which is confirmed by the EBSD phase map, revealing significantly less fcc indexed areas compared to the as deposited state. This can be assigned to partial spinodal decomposition and fcc→w phase transformation, as described in detail in our previous work [8]. Larger zones, which are indexed by EBSD can be related to still intact nanolamellar areas, while non-indexed areas can be attributed to decomposed and transformed fcc→w zones. Although pure w-AlN zones of comparable size might be indexed easily via conventional EBSD, the fine dispersion of globular fcc-TiN particles within the w-AlN matrix seems to impede indexing of w-AlN, while the fcc-TiN globules are too small to be indexed [8]. In particular, next to the substrate larger areas

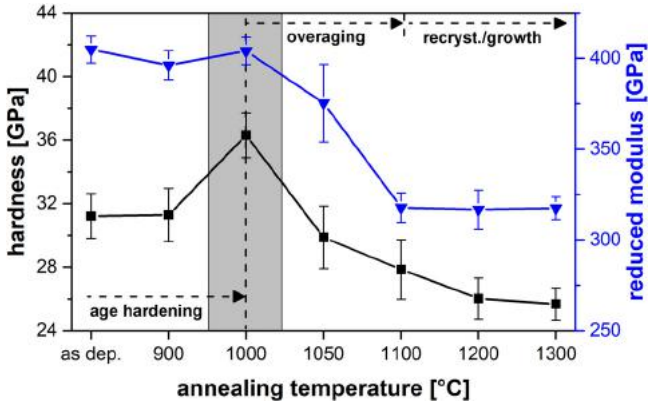

Fig. 3. Global (i.e. surface) hardness and reduced modulus of the CVD fcc-$Ti_{0.2}Al_{0.8}N$ coatings annealed for 5 min in vacuum (obtained by nanoindentation on the coating surface).

of the $Ti_{0.2}Al_{0.8}N$ coating seem to be still intact, whereas the upper part appears to be already mainly decomposed and transformed with minor islands of still intact fcc structure. These observations are corroborated by the corresponding *ex situ* XRD pattern shown in Fig. 2b, which indicates that already significant amounts of w-phase have formed, while still a considerable fraction of fcc-$Ti_{0.2}Al_{0.8}N$ is maintained. It can be concluded that zones with darker contrast within the in-lens SE-SEM image, which correlate with fcc indexed zones in the EBSD map, represent still intact nanolamellar fcc-$Ti_{0.2}Al_{0.8}N$ zones. Non-indexed regions represent already decomposed and transformed fcc-TiN and w-AlN areas, co-existing side by side with the still intact zones [8].

Within the coating annealed at 1200 °C, here considered as final state, the EBSD phase map also only reveals minor fractions of still fcc indexed regions, that cannot unambiguously be correlated with the in-lens SEM image anymore. The corresponding XRD pattern reveals fcc-TiN and w-AlN, while fcc-$Ti_{0.2}Al_{0.8}N$ cannot be clearly identified anymore.

3.3. Evolution of global modulus and hardness after annealing

The evolution of hardness and reduced modulus, investigated by nanoindentation measurements on the surfaces of the samples annealed at different temperatures, is shown in Fig. 3. The trends in hardness and reduced modulus can be consistently correlated with the observed microstructures during annealing. Up to annealing temperatures of 900 °C, no significant changes of microstructure or phase composition were observed. The fcc-$Ti_{0.2}Al_{0.8}N$ grains were still well indexed using EBSD and within SEM images no major changes were found [8]. This is in good agreement with the roughly constant hardness of ~31.5 GPa up to this temperature. After annealing at 1000 °C, the microstructure still remains predominantly fcc, giving good indexing results for EBSD, without any major changes in SEM imaging [8]. However, the hardness shows a maximum of ~36.5 GPa at 1000 °C, which can be explained by the initial spinodal decomposition and the observed maximum in compressive strain as shown in Fig. 1b. The reduced modulus does not reveal any significant changes up to this temperature. After annealing at higher temperatures, the hardness as well as the reduced modulus show a pronounced decrease. This can be explained by the ongoing of fcc→w transformation, resulting in a significantly increased w-phase fraction, and by the decrease of compressive strain. The zone highlighted in grey in Fig. 3 indicates the range within which age hardening will occur. After annealing at 1050 °C, the standard deviation of the reduced modulus shows the highest spread, which is indicative for the highly inhomogeneous microstructure, consisting of still intact fcc areas side by side with decomposed and transformed fcc and w areas. This leads to the assumption that the pronounced anisotropy in microstructure results also in a pronounced anisotropy in mechanical properties on the local scale. Still intact areas most likely retain a high hardness and a reduced modulus comparable to the age hardened state, while decomposed and transformed regions might already exhibit comparatively low values typical for overaged states. If the temperature is further increased, the still intact fcc-fraction diminishes, resulting in a more homogeneous microstructure again (at least on the mesoscopic scale), accompanied by a further decrease of hardness and reduced modulus. The arrows on top of Fig. 3 indicate this region of overaging as well as the range of recrystallization and growth, which is predominantly characterized by microstructural changes, i.e. growth of the precipitates, while the phase composition represents already the final state. Within this range, the reduced modulus remains constant while the hardness still slightly decreases and finally reaches its minimum value of ~26 GPa after annealing at 1300 °C. Similar trends in hardness were previously reported by Todt et al. and Köpf et al. for nanolamellar CVD fcc-$Ti_{1-x}Al_xN$ coatings, who also found annealing temperatures of ~1000 °C to result in maximum hardness, followed by a constant hardness decrease if the temperature is further increased [4,13].

3.4. Cross-sectional modulus mapping after annealing at 1050 °C

A section of the in-lens SE-SEM image of the intermediate state sample covering the ROI is shown in Fig. 4a. Areas with somewhat different contrast, identified as intact fcc zones, are framed by the white dotted lines and fcc as well as fcc+w zones are indexed accordingly. The same section, superimposed by the corresponding EBSD phase map is shown in Fig. 4b. The majority of remaining single phase fcc areas, in particular larger regions, are identified by EBSD and can be clearly correlated with the in-lens SE-SEM image. A minor fraction of presumably remaining fcc zones was not properly indexed via the EBSD measurement, most likely due to the rather small size of the remaining islands and maybe also due to rather high coherency strains, which might negatively affect pattern recognition. Nevertheless, the correlation of in-lens SE-SEM image and EBSD map further supports the identification and interpretation of the individual phase fields within the in-lens SE-SEM image by brightness and contrast. Next to the fcc-TiN baselayer a large fcc zone is observed, which extends at its highest point beyond the discontinuity to ~1/2 of the coating thickness. Above this large fcc phase field, the majority of the coating is defined by decomposed and transformed areas, consisting of w-AlN with embedded globular fcc-TiN precipitates. In addition, smaller single phase fcc fields are still present within larger decomposed and transformed areas, representing small islands of intact nanolamellar structure. Especially in the middle of the image, on top of some grains, significant fcc indexed remains are observed, which are also marked in Fig. 4a. Further, the annealing treatment obviously provoked a certain degree of segregation and agglomeration most probably of fcc-TiN (dark) and w-AlN (bright), as can be concluded from the dark spots (e.g. below the discontinuity) and brighter seams (e.g. along the discontinuity and along grain boundaries).

For the modulus mapping, the ROI was centered and aligned properly using SPM imaging. Subsequently, the dynamic oscillation of the indenter tip was initiated. A 2D map of the recorded displacement amplitude data, which is required to calculate modulus mapping images, is shown in Fig. 4c. Already the contrast within this image indicates significant lateral differences of the elastic properties within the investigated region. In fact, the obtained differences in dynamic displacement seem to correlate well with the identified fcc and fcc+w phase fields. Considering that intact nanolamellar fcc areas coexist with non-lamellar decomposed and transformed fcc+w areas [8], the observed differences in dynamic displacement can be interpreted to represent the differences in moduli of both states. Intact fcc areas that were confirmed via EBSD, still exhibit a relatively high modulus, similar to the as deposited or even age hardened state, consequently resulting in a lower dynamic displacement. In contrast, decomposed and transformed fcc+w areas observe a significantly lower modulus related to a mixture of significant amounts

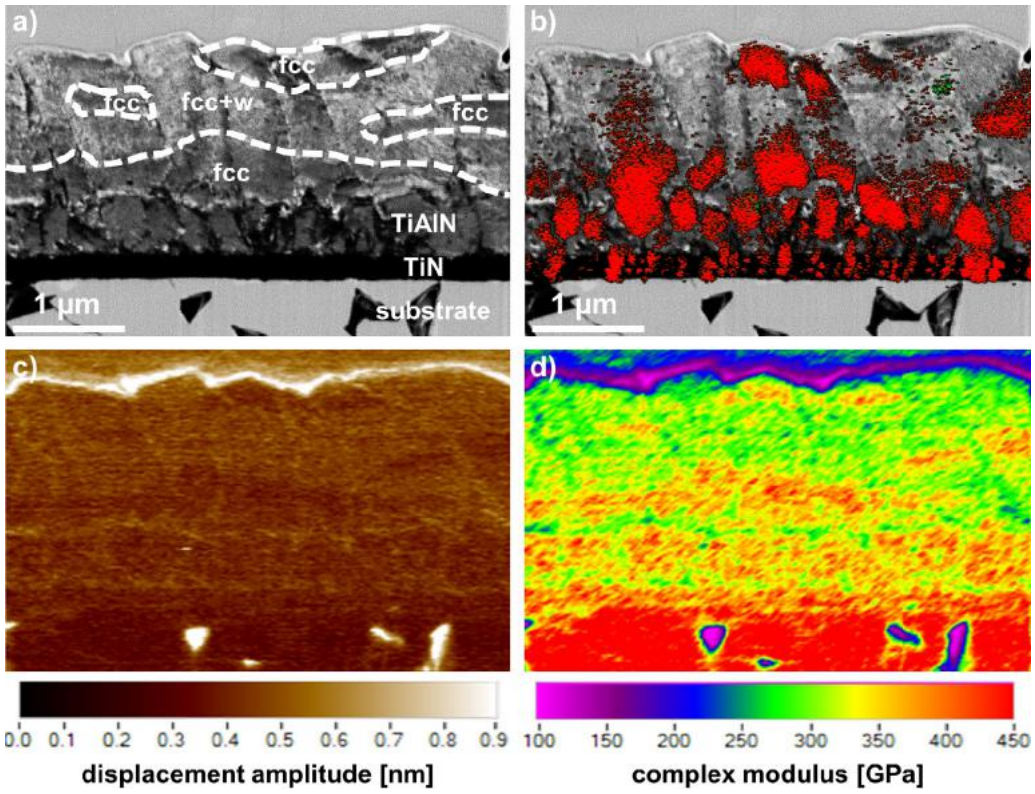

Fig. 4. Contrast enhanced in-lens SE-SEM image (a), superimposed with an EBSD phase map (b), corresponding displacement amplitude map (c) and modulus map (d) of the intermediate state CVD fcc-$Ti_{0.2}Al_{0.8}N$ coating annealed for 5 min at 1050 °C.

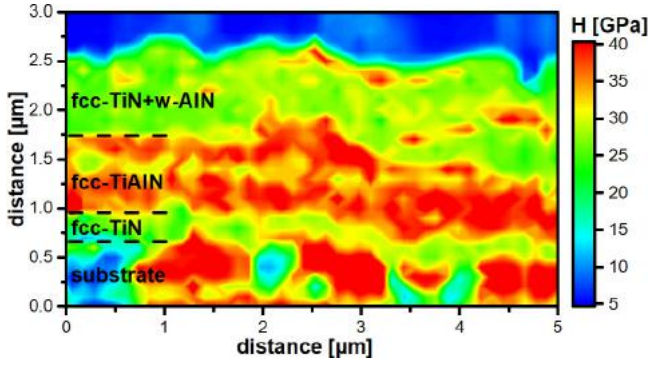

Fig. 5. Hardness map of the intermediate state CVD fcc-$Ti_{0.2}Al_{0.8}N$ coating annealed for 5 min at 1050 °C, obtained by nanoindentation on the coating cross-section.

of w-AlN and some fcc-TiN, thus yielding a much higher dynamic displacement. In addition, the aforementioned local segregations and agglomerations within individual grains, along the discontinuity and along grain boundaries can be identified. Thus already from the displacement amplitude data, a clear correlation of the microstructure and the local elastic properties of the investigated coatings can be deduced. This is confirmed by the evaluation of the modulus mapping measurement, shown in Fig. 4d. It exactly resembles the expected behavior and fits well to the SEM/EBSD investigations. For fcc indexed regions, a complex modulus of slightly above ~400 GPa is estimated and the fcc+w phase fields are estimated to exhibit ~300 GPa. Both values agree well with the values obtained by surface indentation measurements of age hardened and overaged states.

3.5. Cross-sectional hardness mapping after annealing at 1050 °C

Since the observed elastic properties unambiguously correlate with the microstructure of the investigated coating, a similar behavior can also be assumed for the lateral hardness distribution. Intact fcc areas are expected to exhibit a hardness in the range of intact or age hardened TiAlN (~32-36 GPa). In contrast to that, decomposed zones should reveal values corresponding to the overaged or recrystallized state (~24-28 GPa). The results obtained from the hardness mapping are summarized in the contour plot shown in Fig. 5. Similar to the dynamic elastic modulus mapping, the hardness mapping confirms the lateral inhomogeneity caused by the different phase fields. In the substrate, cobalt clusters can be identified, exhibiting a comparatively low hardness compared to the neighboring WC grains. Close to the interface, a continuous layer can be recognized, representing the fcc-TiN baselayer with a moderate hardness of ~22 GPa. The interface appears somewhat curved, which is an artifact stemming from a slight periodic drift of the individual indent lines with respect to their vertical position during the measurement. Above the fcc-TiN baselayer, the intact fcc- $Ti_{0.2}Al_{0.8}N$ area below the discussed discontinuity can be identified, showing a hardness of ~36 GPa, which correlates well with the hardness of the age-hardened state (see Fig. 3). Above this area, the decomposed zone with a significantly lower hardness of ~28 GPa can be seen. Again, this is in accordance with expected values for decomposed and transformed fcc-TiN and w-AlN and agrees well with the global hardness value observed for the overaged state in Fig. 3. Within the predominantly decomposed zone, even the small intact islands, which were detected by EBSD and the modulus mapping, can be identified. In addition, the surface topography of the coating is clearly visible, followed by the soft protective Au layer.

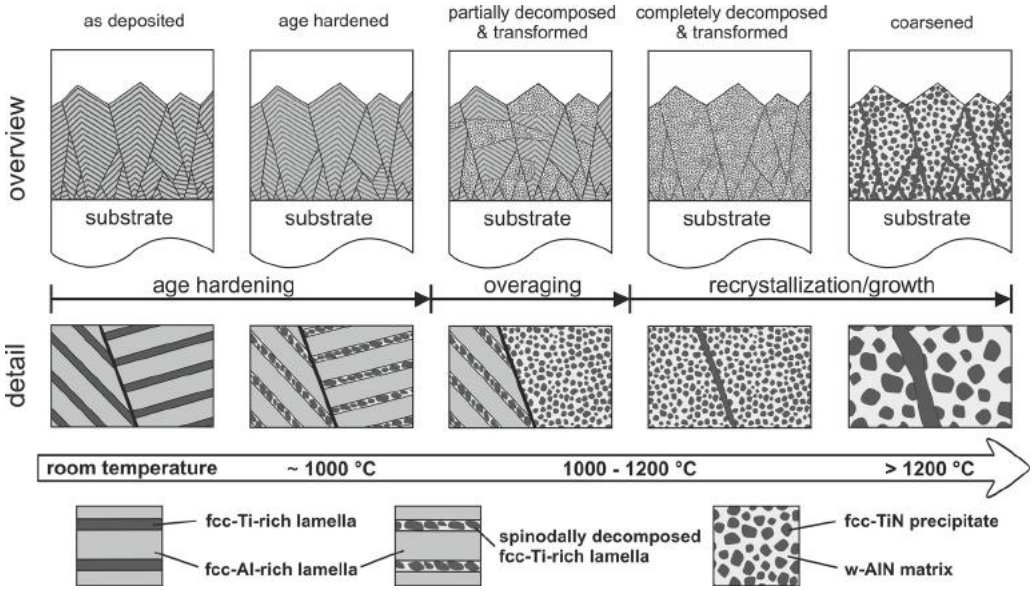

Fig. 6. Schematic microstructural evolution of Al-rich nanolamellar CVD fcc-$Ti_{1-x}Al_xN$ coatings at elevated temperatures.

3.6. Schematic representation of microstructural evolution at elevated temperatures

Considering the results obtained in the present and in our previous study [8], we were able to gain a comprehensive understanding of the spinodal decomposition and fcc→w transformation sequence of nanolamellar CVD fcc-$Ti_{1-x}Al_xN$ coatings at elevated temperatures. The illustration shown in Fig. 6 describes the evolution of the microstructure during annealing starting from the initial state, over spinodal decomposition, which is accompanied by age hardening, to the fcc→w transformation followed by overaging. In the as deposited state, the coating consists of alternating Al-rich and Ti-rich fcc nanolamellae, with a periodicity of several nm. The Ti-rich nanolamellae, representing ~fcc-$Ti_{0.5}Al_{0.5}N$, effectively stabilize the Al-rich species, with a high Al content of ~fcc-$Ti_{0.1}Al_{0.9}N$ [7,8,14]. Since the stabilizing Ti-rich lamellae are significantly thinner than the Al-rich lamellae, as reported in our earlier work [8] and by other authors [4,7,14,15,17], the global Al metal fraction in the coating can be as high as ~0.8, while the coating still maintains a predominantly fcc-structure. Due to their relatively high Al content, the Al-rich lamellae do not show pronounced signs of spinodal decomposition at elevated temperatures. However, the Ti-rich species undergoes spinodal decomposition [8], accompanied by distinctive age hardening due to significantly increased strains. Further increasing the temperature results in the growth of Al-rich clusters within the decomposed Ti-rich lamellae, until they reach a critical size and transform from fcc to their stable w-modification [36]. In further consequence, the formerly stabilized Al-rich lamellae lose their template and larger zones within the coating transform simultaneously, initiated by the newly formed Al-rich clusters. Due to the high global Al-fraction, a w-AlN matrix forms which accommodates globular fcc-TiN precipitates. Previously we could show that those precipitates have a distinct orientation, showing an explicit relation to the w-AlN matrix as well as to the initial nanolamellar fcc-$Ti_{1-x}Al_xN$ grains [8]. On the global scale, the increasing fraction of w-AlN matrix and fcc-TiN particles, which both have a significantly lower hardness and Young´s modulus than the fcc-$Ti_{1-x}Al_xN$, result in a constantly decreasing hardness and Young´s modulus. On the local scale, it needs to be considered that within intermediate sample states, intact nanolamellar areas coexist side by side with completely decomposed and transformed zones. Thus, the global mechanical properties do not thoroughly describe the local mechanical properties, which depend on the lateral distribution of the different phase fields and consequently are highly inhomogeneous. Although the w-AlN matrix with embedded fcc-TiN particles resembles a local inhomogeneity at a much smaller scale, a certain global homogeneity is regained again when the whole coating is fully decomposed and transformed. With further increasing temperature, some fcc-TiN segregates at the grain boundaries and fcc-TiN particles embedded within the matrix grow and accumulate [8]. Simultaneously, the hardness continues to decrease, while the Young´s modulus stays constant. In this condition, at annealing temperatures >1200 °C, the coating can be considered to be in its final microstructural state.

4. Conclusions

Within the present study, the phase and strain evolution of an Al-rich nanolamellar chemical vapor deposited (CVD) face-centered cubic (fcc)-$Ti_{0.2}Al_{0.8}N$ coating at elevated temperatures was determined and correlated with a series of annealed samples, representing different microstructural states. The results corroborate previous findings about the sequence of spinodal decomposition and subsequent fcc→wurtzite (w) transformation of CVD fcc-$Ti_{0.2}Al_{0.8}N$ coatings and could be correlated with age hardening and subsequent overaging. The coating annealed at 1000 °C, which coincides with the temperature that showed the highest compressive strains during the *in situ* synchrotron experiment, exhibited pronounced age hardening and thus, the highest hardness of all samples. With decreasing compressive strain and increasing w-AlN fraction, both, hardness and Young´s modulus significantly declined, which is indicative for overaging. For intermediate sample states, just above the transition from age hardening to overaging, a microstructure composed of nanolamellar fcc phase fields co-existing side by side with non-lamellar decomposed and transformed fcc+w phase fields was observed, suggesting anisotropic lateral mechanical properties. Consequently, cross-sectional SEM/EBSD investigations were employed and correlated with cross-sectional modulus mapping and indentation mapping measurements, to assess the role of the phase fields on local anisotropy and their effect on the global mechanical properties, age hardening and overaging of nanolamellar CVD-$Ti_{0.2}Al_{0.8}N$. Finally, a schematic was created visualizing the microstructural evolution of nanolamellar CVD fcc-$Ti_{1-x}Al_xN$ at elevated temperatures. The obtained results provide the basis for a dedicated nanoscale design of strain and stress, ultimately allowing to create materials with tailored age hardening behavior.

Declaration of Competing Interest

The authors declare that they have no known competing financial interests or personal relationships that could have appeared to influence the work reported in this paper.

Acknowledgments

The authors gratefully acknowledge the financial support under the scope of the COMET program within the K2 Center "Integrated Computational Material, Process and Product Engineering (IC-MPPE)" (Project No 859480). This program is supported by the Austrian Federal Ministries for Transport, Innovation and Technology (BMVIT) and for Digital and Economic Affairs (BMDW), represented by the Austrian research funding association (FFG), and the federal states of Styria, Upper Austria and Tyrol. The financial support by the Austrian Federal Ministry for Digital and Economic Affairs and the National Foundation for Research, Technology and Development is gratefully acknowledged.

References

[1] I. Endler, M. Höhn, M. Herrmann, R. Pitonak, S. Ruppi, M. Schneider, H. van den Berg, H. Westphal, Novel aluminum-rich $Ti_{1-x}Al_xN$ coatings by LPCVD, Surf. Coat. Technol 203 (2008) 530–533.

[2] I. Endler, M. Höhn, M. Herrmann, H. Holzschuh, R. Pitonak, S. Ruppi, H. van den Berg, H. Westphal, L. Wilde, Aluminum-rich TiAlCN coatings by low pressure CVD, Surf. Coat. Technol 205 (2010) 1307–1312.

[3] J. Todt, R. Pitonak, A. Köpf, R. Weißenbacher, B. Sartory, M. Burghammer, R. Daniel, T. Schöberl, J. Keckes, Superior oxidation resistance, mechanical properties and residual stresses of an Al-rich nanolamellar $Ti_{0.05}Al_{0.95}N$ coating prepared by CVD, Surf. Coat. Technol. 258 (2014) 1119–1127.

[4] J. Todt, J. Zalesak, R. Daniel, R. Pitonak, A. Köpf, R. Weißenbacher, B. Sartory, C. Mitterer, J. Keckes, Al-rich cubic $Al_{0.8}Ti_{0.2}N$ coating with self-organized nano-lamellar microstructure: Thermal and mechanical properties, Surf. Coat. Technol. 291 (2016) 89–93.

[5] J. Zalesak, J. Todt, R. Pitonak, A. Köpf, R. Weißenbacher, B. Sartory, M. Burghammer, R. Daniel, J. Keckes, Combinatorial refinement of thin-film microstructure, properties and process conditions: Iterative nanoscale search for self-assembled TiAlN nanolamellae, J. Appl. Crystallogr. 49 (2016) 2217–2225.

[6] A. Paseuth, Y. Kido, S. Imamura, K. Yamagata, A. Miura, K. Tadanaga, Thermal stability and cutting performance of Al-rich cubic $Al_xTi_{1-x}N$ coating prepared by low-pressure chemical vapour deposition, J. Ceram. Soc. Jap. 125 (2017) 913–918.

[7] A. Paseuth, K. Yamagata, A. Miura, M. Higuchi, K. Tadanaga, Deposition and analysis of Al-Rich c-$Al_xTi_{1-x}N$ coating with preferred orientation, J. Am. Ceram. Soc. 100 (2017) 343–353.

[8] M. Tkadletz, C. Hofer, C. Wüstefeld, N. Schalk, M. Motylenko, D. Rafaja, H. Holzschuh, W. Bürgin, B. Sartory, C. Mitterer, C. Czettl, Thermal stability of nanolamellar fcc-$Ti_{1-x}Al_xN$ grown by chemical vapor deposition, Acta Mater 174 (2019) 195–205.

[9] C. Saringer, M. Tkadletz, A. Stark, N. Schell, C. Czettl, N. Schalk, In-situ investigation of the oxidation behavior of metastable CVD $Ti_{1-x}Al_xN$ using a novel combination of synchrotron radiation XRD and DSC, Surf. Coat. Technol. 374 (2019) 617–624.

[10] I. Endler, M. Herrmann, M. Naupert, R. Pitonak, S. Ruppi, M. Schneider, H. van den Berg, H. Westphal, Aluminium-rich $Ti_{1-x}Al_xN$ coatings by CVD, Proc. Euro. PM 2006 (2006) 219–224.

[11] J. Keckes, R. Daniel, C. Mitterer, I. Matko, B. Sartory, A. Koepf, R. Weißenbacher, R. Pitonak, Self-organized periodic soft-hard nanolamellae in polycrystalline TiAlN thin films, Thin Solid Films 545 (2013) 29–32.

[12] A. Köpf, J. Keckes, J. Todt, R. Pitonak, R. Weissenbacher, Nanostructured coatings for tooling applications, Mater. Sci. Forum. 825–826 (2015) 597–604.

[13] A. Köpf, J. Keckes, J. Todt, R. Pitonak, R. Weissenbacher, Nanostructured coatings for tooling applications, Int. J. Refract. Met. Hard Mater 62 (2017) 219–224.

[14] J. Zalesak, D. Holec, I. Matko, M. Petrenec, B. Sartory, N. Koutná, R. Daniel, R. Pitonak, J. Keckes, Peculiarity of self-assembled cubic nanolamellae in the TiN/AlN system: Epitaxial self-stabilization by element deficiency/excess, Acta Mater 131 (2017) 391–399.

[15] M. Meindlhumer, J. Zalesak, R. Pitonak, J. Todt, B. Sartory, M. Burghammer, A. Stark, N. Schell, R. Daniel, J.F. Keckes, M. Lessiak, A. Köpf, R. Wießenbacher, J. Keckes, Biomimetic hard and tough nanoceramic Ti–Al–N film with self-assembled six-level hierarchy, Nanoscale 11 (2019) 7986–7995.

[16] C. Czettl, U. Schleinkofer, F. Schedle, C. Wolf, M. Lechleitner, H. Holzschuh, W. Bürgin, CVD TiAlN – Development and challenges for use in mass production, Proc. 19th Int. Plansee Semin 2017 (2017) 1–13 HM45.

[17] J. Zalesak, M. Bartosik, R. Daniel, C. Mitterer, C. Krywka, D. Kiener, P.H. Mayrhofer, J. Keckes, Cross-sectional structure-property relationship in a graded nanocrystalline $Ti_{1-x}Al_xN$ thin film, Acta Mater 102 (2016) 212–219.

[18] J. Keckes, M. Bartosik, R. Daniel, C. Mitterer, G. Maier, W. Ecker, J. Vila-Comamala, C. David, S. Schoeder, M. Burghammer, X-ray nanodiffraction reveals strain and microstructure evolution in nanocrystalline thin films, Scr. Mater. 67 (2012) 748–751.

[19] P. Sudharshan Phani, W.C. Oliver, A critical assessment of the effect of indentation spacing on the measurement of hardness and modulus using instrumented indentation testing, Mater. Des. 164 (2019) 107563.

[20] E.D. Hintsala, U. Hangen, D.D. Stauffer, High-Throughput Nanoindentation for Statistical and Spatial Property Determination, JOM 70 (2018) 494–503.

[20] H. Neerfeld, The calculation of stress from X-ray elongation measurements, Mitt. KWI Eisenforsch. Dusseld. 24 (1942) 61–70.

[22] R. Hill, The elastic behaviour of a crystalline aggregate, Proc. Phys. Soc. Sect. A. 65 (1952) 349–354.

[23] A.J. Wang, S.L. Shang, Y. Du, Y. Kong, L.J. Zhang, L. Chen, D.D. Zhao, Z.K. Liu, Structural and elastic properties of cubic and hexagonal TiN and AlN from first-principles calculations, Comput. Mater. Sci. 48 (2010) 705–709.

[24] E. Ramos-Moore, C. Espinoza, R.S. Coelho, H. Pinto, P. Brito, F. Soldera, F. Mücklich, J.L. Garcia, Investigations on thermal stresses of a graded Ti(C,N) coating deposited on WC-Co hardmetal, Adv. Mater. Res. 996 (2014) 848–854.

[25] M. Tkadletz, N. Schalk, R. Daniel, J. Keckes, C. Czettl, C. Mitterer, Advanced characterization methods for wear resistant hard coatings: A review on recent progress, Surf. Coat. Technol. 285 (2016) 31–46.

[26] C. Kainz, N. Schalk, M. Tkadletz, C. Saringer, M. Winkler, A. Stark, N. Schell, J. Julin, C. Czettl, Thermo-physical properties of coatings in the Ti(B,N) system grown by chemical vapor deposition, Surf. Coat. Technol. 384 (2020) 125318.

[27] L. Rogström, M.P. Johansson Jõesaar, R. Pilemalm, N. Ghafoor, L.J.S. Johnson, N. Schell, M. Odén, Decomposition routes and strain evolution in arc deposited TiZrAlN coatings, J. Alloy. Compd. 779 (2019) 261–269.

[28] L. Rogström, J. Ullbrand, J. Almer, L. Hultman, B. Jansson, M. Odén, Strain evolution during spinodal decomposition of TiAlN thin films, Thin Solid Films 520 (2012) 5542–5549.

[29] C. Wüstefeld, D. Rafaja, M. Dopita, M. Motylenko, C. Baehtz, C. Michotte, M. Kathrein, Decomposition kinetics in $Ti_{1-x}Al_xN$ coatings as studied by in-situ X-ray diffraction during annealing, Surf. Coat. Technol. 206 (2011) 1727–1734.

[30] R. Rachbauer, S. Massl, E. Stergar, D. Holec, D. Kiener, J. Keckes, J. Patscheider, M. Stiefel, H. Leitner, P.H. Mayrhofer, Decomposition pathways in age hardening of Ti-Al-N films, J. Appl. Phys. 110 (2011) 023515.

[31] P.H. Mayrhofer, A. Hörling, L. Karlsson, J. Sjölén, T. Larsson, C. Mitterer, L. Hultman, Self-organized nanostructures in the Ti–Al–N system, Appl. Phys. Lett. 83 (2003) 2049–2051.

[32] 00-038-1420 PDF, S.D. Gates-Rector, T.N. Blanton, The Powder Diffraction File: A Quality Materials Characterization Database, Powder Diffr. 34 (2019) 352–360.

[33] 00-046-1200 PDF, S.D. Gates-Rector, T.N. Blanton, The Powder Diffraction File: A Quality Materials Characterization Database, Powder Diffr. 34 (2019) 352–360.

[34] 00-025-1133 PDF, S.D. Gates-Rector, T.N. Blanton, The Powder Diffraction File: A Quality Materials Characterization Database, Powder Diffr. 34 (2019) 352–360.

[35] 00-025-1047 PDF, S.D. Gates-Rector, T.N. Blanton, The Powder Diffraction File: A Quality Materials Characterization Database, Powder Diffr. 34 (2019) 352–360.

[36] A. Knutsson, M.P. Johansson, L. Karlsson, M. Odén, Thermally enhanced mechanical properties of arc evaporated $Ti_{0.34}Al_{0.66}N$/TiN multilayer coatings, J. Appl. Phys. 108 (2010) 044312.